Amorphous Lithium Borate Coating Enhances the Electrochemical Performance of Lithium Manganese Iron Phosphate Cathodes for Highly Stable Lithium-Ion Batteries

Seunghyeop Baek, Jihun Roh, Jangwook Pyun, Yeon-U Lee, Sangki Lee, Seung-Tae Hong, Namhyung Kim,* and Munseok S. Chae*

The advancement of high-voltage lithium-ion batteries necessitates the use of cathode materials with improved electrochemical performance and cycling stability. Herein, an amorphous $Li_2B_4O_7$ coating effectively enhances the electrochemical properties of $LiMn_{0.6}Fe_{0.4}PO_4$ (LMFP) cathodes is demonstrated. Specifically, the $Li_2B_4O_7$ layer improves lithium-ion conductivity while suppressing manganese dissolution induced by Jahn-Teller distortion, both of which are critical factors affecting LMFP stability. Structural and electrochemical analyses reveal that the amorphous coating reduces Coulomb repulsion, lowers the energy barrier for lithium-ion migration, and enhances charge transfer kinetics. The coated LMFP demonstrates a high discharge capacity of 143.9 mAh g^{-1} at 20 mA g^{-1} and exhibits excellent cycling stability, retaining 94.6% of its capacity after 1000 cycles at 600 mA g^{-1}. Furthermore, the amorphous $Li_2B_4O_7$ coating enhances rate capability by facilitating rapid ion transport. These findings underscore the potential of $Li_2B_4O_7$ as a multifunctional coating material for advanced lithium-ion battery cathodes, presenting a scalable and effective strategy for next-generation energy storage applications.

1. Introduction

With increased focus on overcoming fossil fuel dependence and the associated environmental pollution, efforts to identify alternative energy sources have intensified. Among the various energy storage systems available, lithium-ion batteries (LIBs) have emerged as one of the most promising candidates owing to their high energy density, long cycle life, and relatively eco-friendly design.[1] LIBs are widely employed in diverse applications, including portable electronic devices, electric vehicles, and hybrid cars. However, the growing demand for enhanced performance and stability in LIBs presents significant challenges, underscoring the necessity for the development of new materials and structural innovations.[2–5]

Among the various cathode materials used in LIBs, nickel-cobalt-manganese (NCM) compounds are a preferred choice and extensively utilized owing to their high energy density.[6,7] Despite the superior energy density of NCM materials, their cost-effectiveness remains a significant limitation. Consequently, lithium iron phosphate (LFP), characterized by its olivine structure, has garnered attention for its superior cost efficiency.[8] Additionally, LFP offers several benefits, including high electrical and thermal safety as well as environmental friendliness.[9] Nevertheless, LFP is constrained by its relatively low operating voltage of ≈3.4 V compared to the lithium (Li/Li+) standard.

As global energy demands continue to escalate, lithium manganese iron phosphate (LMFP) has emerged as a compelling alternative to LFP.[10–12] LMFP provides a higher operating voltage of ≈4.0 V (vs. Li/Li$^+$), making it particularly advantageous for applications requiring enhanced energy performance. However, incorporating manganese (Mn) into the LMFP structure introduces significant challenges. Specifically, Mn induces structural instability due to Jahn-Teller distortion, which compromises cycle stability and restricts the overall lifespan of the battery.[13–15]

Despite these challenges, extensive research has been conducted to overcome the limitations of LMFP. Various strategies have been investigated to enhance its electrochemical performance, with one of the most promising approaches being

S. Baek, J. Pyun, S. Lee, M. S. Chae
Department of Nanotechnology Engineering
Pukyong National University
Busan 48513, Republic of Korea
E-mail: mschae@pknu.ac.kr

J. Roh, Y.-U. Lee, S.-T. Hong
Department of Energy Science and Engineering
DGIST
Daegu 42988, Republic of Korea

S.-T. Hong
Department of Chemistry and Chemical Biology
University of New Mexico
New Mexico 87131, United States

N. Kim
Department of Materials System Engineering
Pukyong National University
Busan 48513, Republic of Korea
E-mail: namhyung.kim@pknu.ac.kr

cathode surface coating.[16] This technique is designed to mitigate structural instability arising from manganese dissolution, improve electrochemical properties, and extend both cycle stability and battery lifespan.

Various coating materials, such as titanium dioxide (TiO_2),[17] aluminum oxide (Al_2O_3),[18] aluminum fluoride (AlF_3),[19] and zinc oxide (ZnO),[20] have been investigated for their ability to enhance the electrochemical performance of cathode materials. These non-lithium-containing compounds primarily function as protective barriers, preventing manganese dissolution by shielding the host structure. However, a major limitation of these coatings is their tendency to hinder lithium-ion diffusion, which can degrade overall battery performance.[21] To address this limitation, coating with lithium-containing oxides has been proposed.[22] Such coatings are expected to facilitate lithium-ion conductivity, thereby improving ionic conductivity and enhancing the overall electrochemical performance of the battery.

Among the various candidates, lithium boron oxide polymorphs have demonstrated exceptional effectiveness in enhancing both cycle stability and electrochemical performance.[23,24] Prior to experimental testing, we performed diffusion barrier and pathway analyses of the $Li_2B_4O_7$ structure using the soft-BV method (**Figure 1**a).[25,26] Based on the analysis results, the $Li_2B_4O_7$ structure demonstrates excellent lithium-ion conductivity, facilitated by a three-dimensional Li-ion diffusion network (Figure 1b). This structure features two distinct types of diffusion barriers: one within the diffusion cavity (Figure 1c) and the other at a bottleneck point (Figure 1d). The calculated lithium migration barriers for these pathways were 0.206 eV and 0.280 eV, respectively (Figure 1e), which are typical values for lithium diffusion activation barriers in battery materials. These findings underscore

the potential of $Li_2B_4O_7$ as a highly suitable coating material for LMFP.

Further, to assess the suitability of this composition as a coating material based on its crystallinity, we investigated both amorphous and crystalline $Li_2B_4O_7$ coatings. We hypothesized that the defect-rich nature of the amorphous phase, attributed to oxygen vacancies, would facilitate Li-ion migration. Additionally, lithium transport in both crystalline and amorphous phases has been the focus of extensive recent research.[27]

In this study, we present amorphous $Li_2B_4O_7$-coated LMFP as a highly stable cathode material for LIBs, marking its first reported application. To elucidate the lithium diffusion mechanism in $Li_2B_4O_7$, we conducted a comprehensive investigation incorporating electrochemical, structural, elemental, spectroscopic, and lithium diffusion path analyses. Our findings underscore the pivotal role of multifunctional coatings in enhancing the cycle stability and electrochemical performance of LMFP, highlighting their significance in advancing energy storage efficiency and longevity.

2. Results and Discussion

2.1. Material Synthesis and Characterization

The synthesis procedure is illustrated in **Figure 2**. Specifically, $LiFe_{0.4}Mn_{0.6}PO_4$ powders were synthesized via a sol–gel method using Li_2CO_3 (99%, Sigma-Aldrich), $FeC_2O_4 \cdot 2H_2O$ (99%, Sigma-Aldrich), $Mn(COOCH_3)_2 \cdot 4H_2O$ (99%, Sigma-Aldrich), and $NH_4H_2PO_4$ (99.5%, Sigma-Aldrich) as precursors. These reagents were dissolved in deionized water at room temperature, followed by continuous magnetic stirring and drying at 60 °C overnight to remove
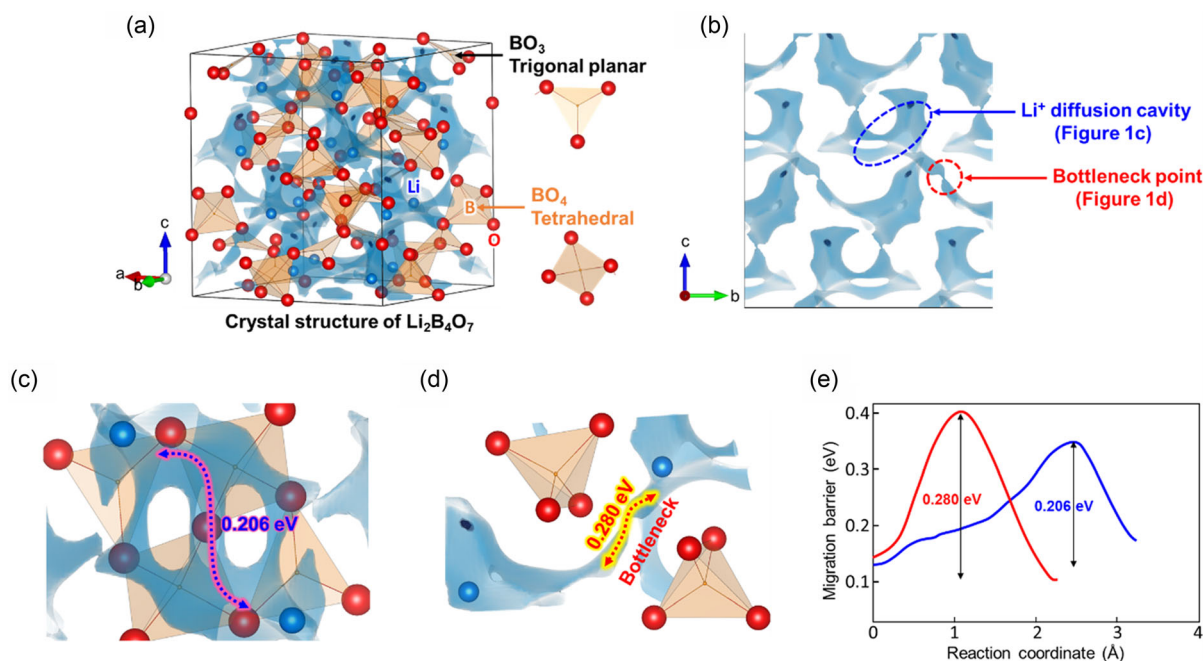

Figure 1. a) Crystal structure of $Li_2B_4O_7$ along with the corresponding lithium-ion migration pathways; b) visualization of the lithium-ion pathways within the bc-plane, shown without the structural framework for clarity; detailed view of the local lithium-ion pathways, highlighting c) the cage sites and d) bottleneck points; e) migration barrier for lithium ions in $Li_2B_4O_7$.
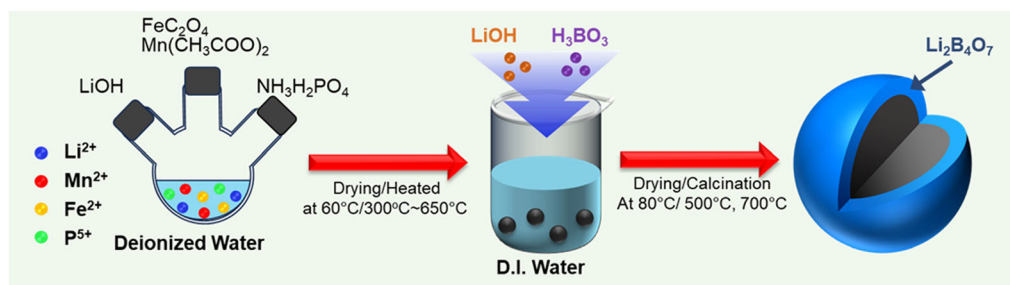
Batteries & Supercaps

Research Article
doi.org/10.1002/batt.202500207

Chemistry Europe
European Chemical
Societies Publishing

Figure 2. Schematic representation of the synthesis process for LMFP-Li$_2$B$_4$O$_7$ particles.

residual moisture. The dried powders were then calcined at 650 °C under an Ar atmosphere to obtain carbon-coated LMFP. The obtained carbon-coated LMFP powders were coated with Li$_2$B$_4$O$_7$ (LBO) via a sol–gel method. For the LBO coating, LiOH (98%, Sigma-Aldrich) and H$_3$BO$_3$ (99.5%, Sigma-Aldrich) were dissolved in deionized water at a molar ratio of 1:2. Subsequently, 10 g of LMFP was added to the prepared solution, ensuring an LBO content of 1 wt% relative to the LMFP. The resulting mixture was stirred at 200 rpm and dried overnight at 80 °C. The dried powders were then subjected to sequential heat treatments at 500 °C and 700 °C for 20 min each under Ar atmosphere.

To characterize the synthesized materials, scanning electron microscopy (SEM), transmission electron microscopy (TEM) with energy-dispersive X-ray spectroscopy (TEM-EDX), X-ray diffraction (XRD), and X-ray photoelectron spectroscopy (XPS) analyses were performed. The surface morphologies of pristine LMFP, LMFP-LBO500 (LBO coated at 500 °C), and LMFP-LBO700 (LBO coated at 700 °C) observed via SEM are shown in Figure 2a–c and S1-2, Supporting Information. The particle sizes across all samples were ≈200 nm; however, distinct morphological differences were observed. Notably, the LBO-coated samples exhibited rougher surfaces than pristine LMFP, a feature attributed to the LBO coating layer. Additionally, while the pristine and LMFP-LBO500 samples displayed comparable particle morphologies, LMFP-LBO700 demonstrated enhanced particle connectivity due to the effects of high-temperature calcination.

The presence of the amorphous LBO coating layer was confirmed via TEM, as shown in **Figure 3**d,e. A uniform LBO layer with a thickness of ≈5 nm was observed on the LMFP particles. Elemental mapping confirmed the homogeneous distribution of boron and oxygen across the entire surface, particularly in the LMFP-LBO500 sample (Figures 3f and S3, Supporting Information), indicating consistent coating quality. Although direct Li$^+$ flux measurement through the coating is not feasible, enhanced diffusion-controlled behavior observed in the CV and b-value analyses (vide infra, Figure 6) indirectly substantiates the ion-conductive role of the LBO layer, which has already been discussed in several previous reports.[28,29] However, the coating morphology varied with the calcination temperature. The sample treated at 500 °C exhibited a uniformly coated surface, while the sample treated at 700 °C displayed an island-type growth with a rougher coating layer. TEM-EDX elemental mapping of LMFP-LBO500 and LMFP-LBO700 (Figure 3f and S3, Supporting Information) further confirmed the presence of the LBO layer,

with boron (B) and oxygen (O) signals uniformly distributed on the LMFP surface. In contrast, the pristine sample lacked a detectable boron signal, as shown in Figure S4, Supporting Information.

XRD patterns of the samples (Figure 3g) revealed no significant differences between the pristine and LBO-coated powders, suggesting that the LBO phase is amorphous. An enlarged view of the XRD patterns (Figure 3h) showed slight peak broadening, which can be attributed to the presence of the amorphous LBO phase. XPS analysis (Figure 3i) further corroborated these findings, confirming the presence of boron in the LBO-coated samples. The boron signal intensity varied with calcination temperature, suggesting that boron exists in different chemical states in the LMFP-LBO500 and LMFP-LBO700 samples.

Although the precursor ratio and synthesis conditions were optimized to form a Li$_2$B$_4$O$_7$-like network, also possible coexistence of other lithium boron oxide polymorphs (e.g., LiBO$_2$, Li$_3$BO$_3$), as evidenced by the B 1s XPS spectra (Figure 3i), which display peak splitting indicative of multiple B–O coordination environments (BO$_3$ and BO$_4$ units) consistent with amorphous borates.[30] However, when we calcine only coating solution, it formed low crystalline and high crystalline Li$_2$B$_4$O$_7$ phases at 500 °C and 700 °C, respectively (Figure S5, Supporting Information). While EDX mapping (Figure 3f and S3, Supporting Information) confirms the presence of boron on the particle surface and reveals no detectable Mn or Fe signals on the coating, the incorporation of trace transition metal cations or boron diffusion into the LMFP bulk during high-temperature treatment cannot be completely excluded.[31] The absence of secondary phases or lattice distortion in the XRD patterns (Figure 3g) suggests minimal B incorporation into the LMFP crystal structure under current conditions. Nonetheless, subtle doping effects or interfacial diffusion phenomena may exist.

To investigate the crystallinity of LBO, various spectroscopic analyses were conducted. As shown in the Fourier transform infrared spectroscopy (FTIR) spectrum (**Figure 4**a), pristine LMFP exhibits a broad absorption peak near 1000 cm^{-1}.[32] The spectrum closely resembled that of pristine LMFP, indicating that the LBO layer remained amorphous, with no detectable B—O bond signals. In contrast, calcination at 700°C produced a distinct B—O peak at 1211 cm^{-1},[33] suggesting the crystallization of the LBO layer at this temperature. Raman spectroscopy analysis (Figure 4b) revealed a Fe—O peak at 585 cm^{-1}, an Mn—O peak at 648 cm^{-1}, and a PO$_4^{3-}$ peak at 947 cm^{-1}, confirming their association with the pristine LMFP spectrum.[34] Following LBO
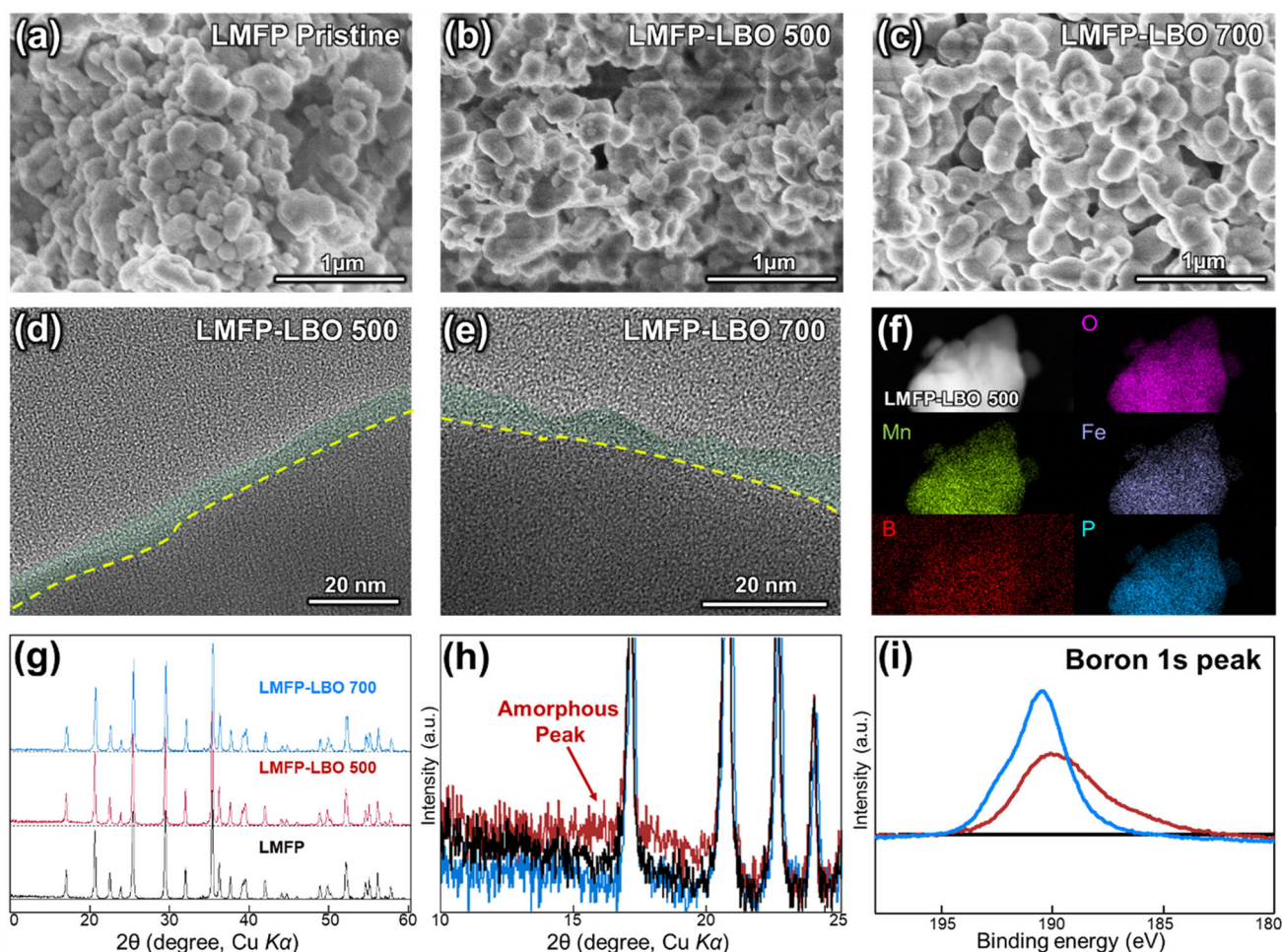
Figure 3. SEM images of a) pristine LMFP, b) LMFP-LBO500, and c) LMFP-LBO700; TEM images of d) LMFP-LBO500 and e) LMFP-LBO700; f) EDX elemental mapping of LMFP-LBO500; g) XRD patterns of pristine LMFP, LMFP-LBO500, and LMFP-LBO700; h) B 1s XPS spectra of pristine LMFP, LMFP-LBO500, and LMFP-LBO700 samples; i) XPS analysis.
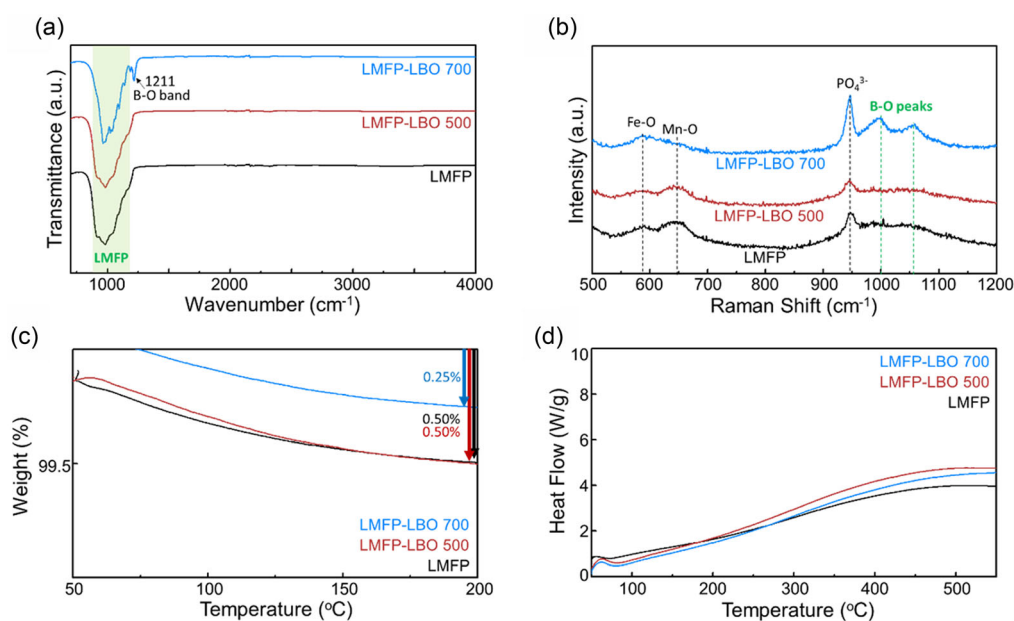

Figure 4. a) FTIR-ATR spectra and b) Raman spectra of pristine LMFP, LMFP-LBO500, and LMFP-LBO700; c) TG and d) DSC curves of pristine LMFP, LMFP-LBO500, and LMFP-LBO700; temperature scan rate: 5 °C min.

Batteries & Supercaps

Research Article
doi.org/10.1002/batt.202500207

Chemistry Europe
European Chemical
Societies Publishing

calcination at 500 °C, no notable shifts or additional Raman peaks were observed, consistent with the preservation of an amorphous LBO layer. However, after calcination at 700 °C, new B—O bond peaks emerged at ≈1000 and 1053 cm^{-1}.[35] These findings align with the FTIR results, indicating the presence of an amorphous LBO layer at 500 °C and the crystallization of the LBO layer at 700 °C. In addition, we observed that the intensities of the Mn—O, Fe—O, and PO_4^{3-} Raman peaks increase upon calcination at 700 °C compared to both the pristine LMFP and LMFP–LBO500 samples. It is plausible that the elevated calcination temperature facilitated partial crystallization or ordering of the LMFP core itself, thereby enhancing its crystallinity.

Thermogravimetric analysis (TGA) and differential scanning calorimetry (DSC) were performed to assess the thermal stability of all samples. The TGA results revealed a minor weight loss with increasing temperature; however, the loss was negligible, confirming that LBO-coated LMFP remains thermally stable below 200 °C (Figure 4c). Furthermore, the DSC curves of all samples exhibited similar heat flow behavior (Figure 4d), indicating the absence of significant exothermic peaks or thermal decomposition up to 200 °C in the LBO-coated samples.

2.2. Electrochemical Characterization

All electrochemical measurements were performed using a standard two-electrode configuration. The LMFP, LMFP-LBO500, and LMFP-LBO700 electrodes served as the working electrodes, while lithium metal functioned as both the counter and reference electrode. A 1.3 M LiPF$_6$ electrolyte solution, prepared in a mixture of ethylene carbonate (EC), ethyl methyl carbonate (EMC), and diethyl carbonate (DEC), was used as the electrolyte.

Cyclic voltammetry (CV) measurements were conducted at a scan rate of 0.2 mV·s^{-1} within the voltage range of 2.8–4.5 V versus Li/Li$^+$ to assess the electrochemical redox behavior of the electrodes (**Figure 5**a). The CV curves of LMFP, LMFP-LBO 500, and LMFP-LBO 700 display characteristic redox peaks corresponding to the Fe^{2+}/Fe^{3+} ≈3.4 V) and Mn^{2+}/Mn^{3+} (≈3.9 V) redox couples. Additionally, an extra peak appears at ≈3.5 V, which may originate from the randomly ordered Mn–Fe structure, a phenomenon commonly reported in the literature.[11] Notably, the LBO-coated samples annealed at 500 °C exhibit increased peak currents relative to pristine LMFP, suggesting enhanced electrochemical performance. This improvement is attributed to the amorphous nature of the LBO coating, which facilitates superior ionic and electronic conductivity.

Galvanostatic charge–discharge (GCD) measurements were performed at current densities of 20 mA g^{-1} and 600 mA g^{-1} to further assess the electrochemical performance of the electrodes (Figure 5b). At a low current density of 20 mA g^{-1}, all samples exhibited a discharge capacity of ≈144 mAh·g^{-1}. However, under high-rate charge–discharge conditions at 600 mA g^{-1}, pristine LMFP delivered a significantly lower discharge capacity of 51.0 mAh g^{-1}, whereas LMFP-LBO 500 and LMFP-LBO 700 exhibited enhanced capacities of 67.3 mAh g^{-1} and 58.7 mAh g^{-1}, respectively. These results suggest that the LBO coating facilitates improved charge transport kinetics, enabling more efficient charge–discharge processes under high-current conditions. The rate performance of the electrodes was further examined across increasing current densities (Figure 5c). A gradual decrease in capacity was observed with rising current density, a trend consistent with lithium-ion diffusion limitations. Notably, LMFP-LBO 500 demonstrated superior rate capability compared to both
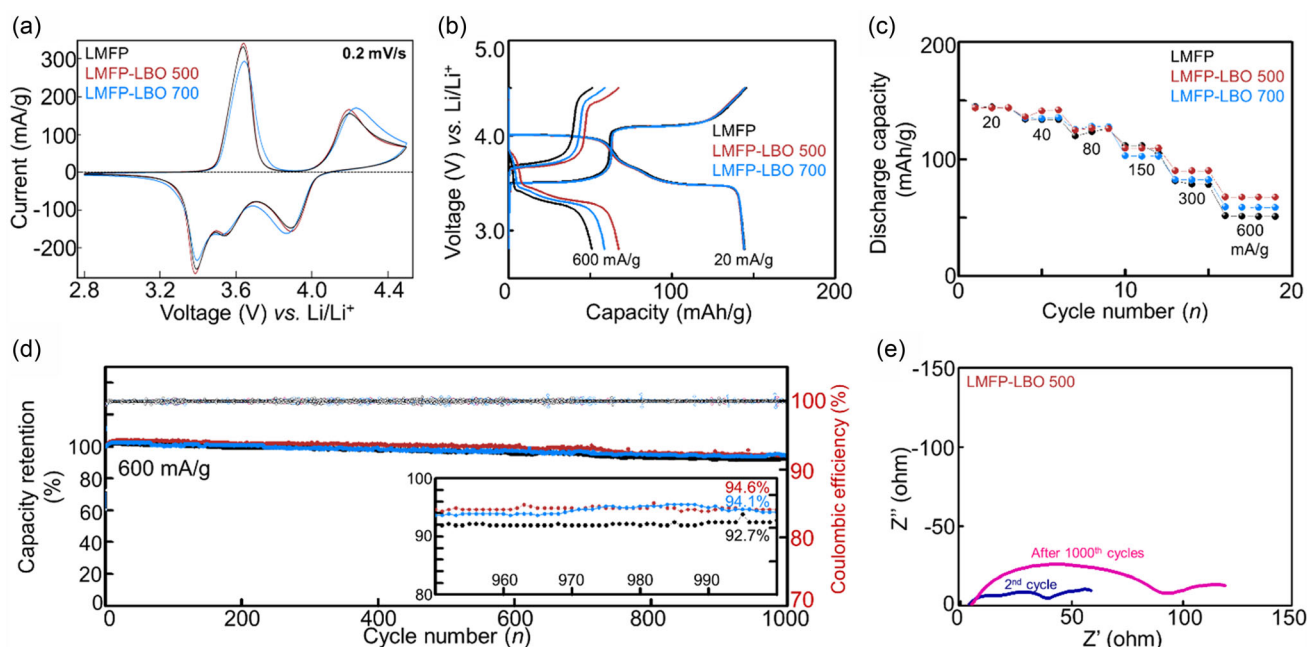

Figure 5. Electrochemical characterizations for LMFP, LMFP-LBO 500, and LMFP-LBO 700 electrodes: a) CV curves at a scan rate of 0.2 mV s^{-1}, b) GCD profiles at 20 and 600 mA g^{-1} current, c) rate capabilities, and d) long-term cycling performance and Coulombic efficiency; e) impedance spectra of before and after cycled LMFP-LBO 500 cells.
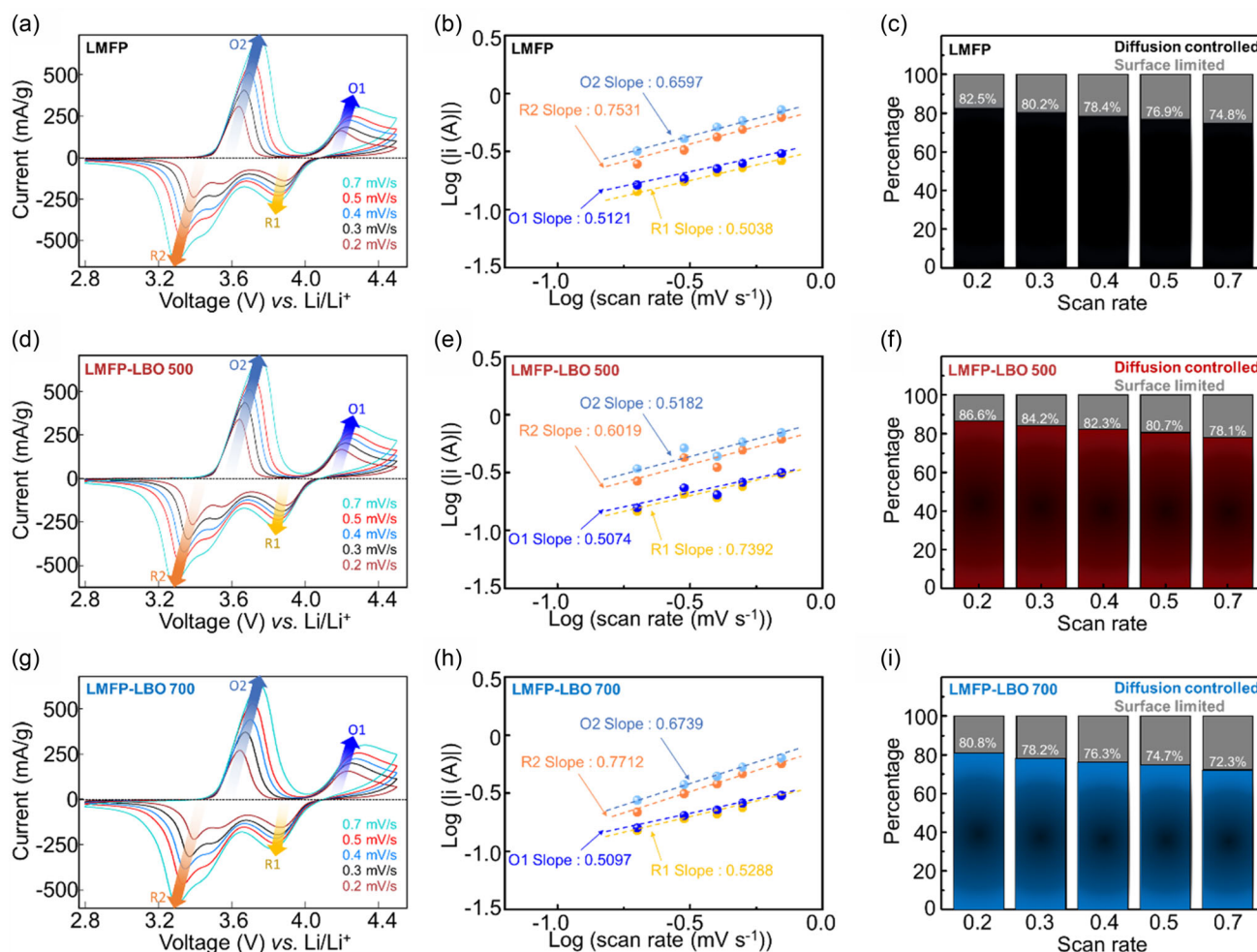
Batteries & Supercaps

Research Article
doi.org/10.1002/batt.202500207

Chemistry Europe
European Chemical
Societies Publishing

Figure 6. CV curves measured at scan rates from 0.2 to 0.7 mV·s^{-1} for a) pristine LMFP, d) LMFP-LBO 500, and g) LMFP-LBO 700, respectively, Calculation of b-values based on the relationship between specific cathodic peak current and scan rate for b) pristine LMFP, e) LMFP-LBO 500, and h) LMFP-LBO 700, calculated of surface-limited and diffusion-controlled ion reaction ratios for c) pristine LMFP, f) LMFP-LBO 500, and i) LMFP-LBO 700, respectively.

LMFP-LBO 700 and pristine LMFP, confirming the effectiveness of the LBO coating in enhancing electrochemical kinetics. A comprehensive analysis of GCD profiles at various current densities (20, 40, 80, 150, 300, and 600 mA g^{-1}) is provided in Figure S6–S8, Supporting Information.

Long-term cycling tests were performed at a current density of 600 mA g^{-1} to assess the durability of the electrodes over extended cycling (Figure 5d). After 1000 cycles, LMFP-LBO 500 exhibited the highest capacity retention of 94.6%, followed by LMFP-LBO 700 (94.1%) and pristine LMFP (92.7%). Additionally, all samples maintained a Coulombic efficiency of ≈100%, confirming the stability of the electrodes during prolonged cycling. The enhanced cycling performance of the LBO-coated electrodes is attributed to the protective nature of the LBO layer, which suppresses Mn dissolution associated with Jahn-Teller distortion in the LMFP cathode. Although the suppression of Mn dissolution is supported by the enhanced capacity retention (Figure 5d) and preserved structural integrity (Figure S15, Supporting Information), we further confirmed this by directly quantifying Mn^{2+} in the electrolyte via ICP-OES, which revealed that the LBO-coated sample exhibited significantly lower Mn dissolution compared to the pristine counterpart (Table S1, Supporting Information).

Electrochemical impedance spectroscopy measurements were performed before and after 1000 cycles to analyze the charge transfer characteristics of LMFP-LBO 500 (Figure 5e). The Nyquist plots were analyzed using a modified equivalent circuit that decouples the surface film resistance (R_{SEI}) and charge transfer resistance (R_{ct}) components. After 1000 cycles, R_{IR} increased from 4.72 to 5.8 Ω, and R_{ct+SEI} rose from 40.3 Ω to 93.4 Ω. The overall rise in resistance is likely due to a combination of interfacial degradation and diminished reaction kinetics. Additionally, EIS comparisons with pristine LMFP (Figure S9, Supporting Information) confirm that the LBO coating effectively reduces the initial interfacial resistance, supporting its role in enhancing interfacial charge transfer and mitigating CEI formation during early cycling.

Electrochemical evaluations reveal that amorphous LBO coatings outperform crystalline counterparts owing to the following advantages:[36] 1) Reduced bandgap and enhanced conductivity—amorphous materials facilitate accelerated electron transfer, which is attributed to their lower bandgap, leading

Batteries & Supercaps

Research Article
doi.org/10.1002/batt.202500207

Chemistry
Europe
European Chemical
Societies Publishing

to improved electrical conductivity. Qin et al. demonstrated that amorphous $Zn_2V_2O_7$ possesses a narrower bandgap than its crystalline form, thereby promoting more efficient charge transport.[37] 2) Lower energy barrier for lithium-ion transport—the disordered structure of amorphous materials reduces Coulomb repulsion between lithium ions, thereby lowering the energy barrier for ion migration.[27,38–40] This property enhances lithium-ion conductivity and structural stability while minimizing resistance buildup during repeated charge–discharge cycles. 3) Mitigation of volume expansion—the flexible and disordered nature of amorphous materials effectively accommodates mechanical strain caused by lithium intercalation and deintercalation.[41] This structural adaptability minimizes stress-induced degradation, preserving electrode integrity and enhancing electrochemical performance over prolonged cycling. These key factors highlight the advantages of amorphous LBO coatings in enhancing lithium-ion battery performance, positioning them as a promising strategy for advanced cathode materials. While the stable cycling performance and preserved lattice structure suggest the suppression of Jahn-Teller distortion, more direct evidence could be obtained through in-situ techniques such as in situ XRD and extended X-ray absorption fine structure. These operando analyses will be conducted in future studies to validate the distortion-mitigation effect of the LBO coating.

To further investigate the Li-ion storage mechanism of LMFP, LMFP-LBO 500, and LMFP-LBO 700, CV measurements were performed at scan rates ranging from 0.2 to 0.7 mV s (**Figure 6**a,d,g). Power-law analysis was applied to differentiate between surface-limited capacitive behavior and diffusion-controlled kinetics. In this method, a b-value close to 0.5 signifies a diffusion-controlled intercalation process, whereas a value approaching 1 suggests a surface-limited reaction. The calculated b-values for the oxidation and reduction peaks of each sample are as follows: For pristine LMFP, the O1, O2, R1, and R2 peaks exhibited slopes of 0.5121, 0.6597, 0.5038, and 0.7531, respectively (Figure 6b). In contrast, LMFP-LBO 500 displayed increased b-values, with O1, O2, R1, and R2 peaks at 0.5074, 0.5182, 0.7392, and 0.6019, respectively, indicating a greater contribution from diffusion-controlled intercalation processes (Figure 6e). Meanwhile, LMFP-LBO 700 exhibited a lower diffusion-controlled response, with corresponding b-values of 0.5097, 0.6739, 0.5288, and 0.7712 (Figure 6h).

Further analysis of the capacitive and diffusion-controlled contributions was conducted, and the detailed calculations are provided in Figure S10–S12, Supporting Information. The results indicate that for pristine LMFP, diffusion-controlled intercalation accounted for ≈82.5% at a scan rate of 0.2 mV s^{-1}, gradually decreasing to 74.8% at 0.7 mV s^{-1} (Figure 6c). Among the samples, LMFP-LBO 500 exhibited the highest intercalation contribution, ranging from 86.6% at 0.2 mV s^{-1} to 78.1% at 0.7 mV s^{-1} (Figure 6f), strongly supporting the role of the amorphous LBO coating in facilitating rapid ion transport. This enhancement in ion diffusivity contributes to improved charge storage kinetics, particularly at high scan rates, highlighting its superior fast charge-discharge capability. In contrast, LMFP-LBO 700 exhibited a lower diffusion-controlled contribution, with values decreasing from 80.8% at 0.2 mV s^{-1} to 72.3% at 0.7 mV s^{-1} (Figure 6i), showing a behavior comparable to or slightly lower than that of pristine LMFP.

These results indicate that LMFP with an amorphous LBO coating primarily exhibits diffusion-controlled behavior. This phenomenon is likely due to the enhanced surface ion diffusivity and improved charge transfer kinetics facilitated by the LBO layer, which collectively contribute to superior electrochemical performance under high-rate conditions.

To further elucidate the Li-ion transport kinetics, galvanostatic intermittent titration technique (GITT) was employed to determine the lithium diffusion coefficients of the pristine and coated electrodes. As shown in Figure S13, Supporting Information the LMFP–LBO500 electrode exhibited a slightly higher diffusion coefficient (≈6.96×10^{-11} cm^2 s^{-1}) compared to pristine LMFP (≈5.45×10^{-11} cm^2 s^{-1}). These findings clearly demonstrate the beneficial effect of the amorphous LBO coating in promoting rapid ion transport, which is consistent with the observed enhancement in rate capability.

Although the LBO coating is primarily designed to enhance lithium-ion transport, its impact on electronic conductivity remains unclear. Given the low electronic conductivity of borate glasses, the improved rate capability likely stems from enhanced ionic mobility.[36] However, possible interfacial electronic contributions cannot be excluded. Further studies using four-point probe or temperature-dependent impedance spectroscopy are needed to assess the transport properties in detail.

All XPS core-level spectra were subjected to peak fitting, and the results are presented in **Figure 7**. Distinct signals corresponding to Li_2CO_3 and $ROCO_2Li$ were clearly resolved. Notably, the intensity of the LiF peak was reduced after LBO coating. Additionally, the PO_4^{3-} peaks became broadened after cycling in the pristine sample, whereas they remained well defined and stable in the LBO-coated electrode. To investigate the formation of the CEI on the LMFP-LBO 500 cathode surface after 1000 cycles, XPS analysis was conducted. As presented in Figure 7a, the C 1s spectrum exhibits a characteristic peak at ≈290 eV, corresponding to the presence of a C=O bond, which is typically associated with the formation of lithium carbonate (Li_2CO_3) or lithium alkyl carbonate ($ROCO_2Li$).[42] Additionally, FTIR corroborates the formation of Li_2CO_3 and $ROCO_2Li$, further supporting the XPS findings (Figure S14, Supporting Information). The F 1s spectrum shown in Figure 7b reveals a fluorine-organic signal at 687 eV, indicating the possible formation of lithium fluoride (LiF) or fluorine-containing organic compounds.[42] In addition, the fluorine signal originates from the electrolyte salt, lithium hexafluorophosphate ($LiPF_6$). Figure 7c confirms the presence of an O 1s peak, with a metal–oxygen (M—O) bond observed at ≈532.5 eV, primarily attributed to Li_2CO_3.[42] Furthermore, the Li 1s spectrum in Figure 7d confirms the incorporation of lithium species, further supporting the formation of a lithium-containing CEI layer.

A comparative analysis between the uncoated and LBO-coated samples after cycling reveals clear differences in structural and interfacial stability. The cycled pristine LMFP exhibited pronounced peak broadening in XRD, intensified Li_2CO_3 and $ROCO_2Li$ signals in FTIR, and notable disruption of the PO_4^{3-} framework as evidenced by changes in the P 2p XPS spectrum (Figure 7e). In contrast, the LMFP–LBO500 sample maintained well-defined P 2p peaks and showed significantly reduced carbonate formation. These results highlight the effectiveness of the LBO coating in
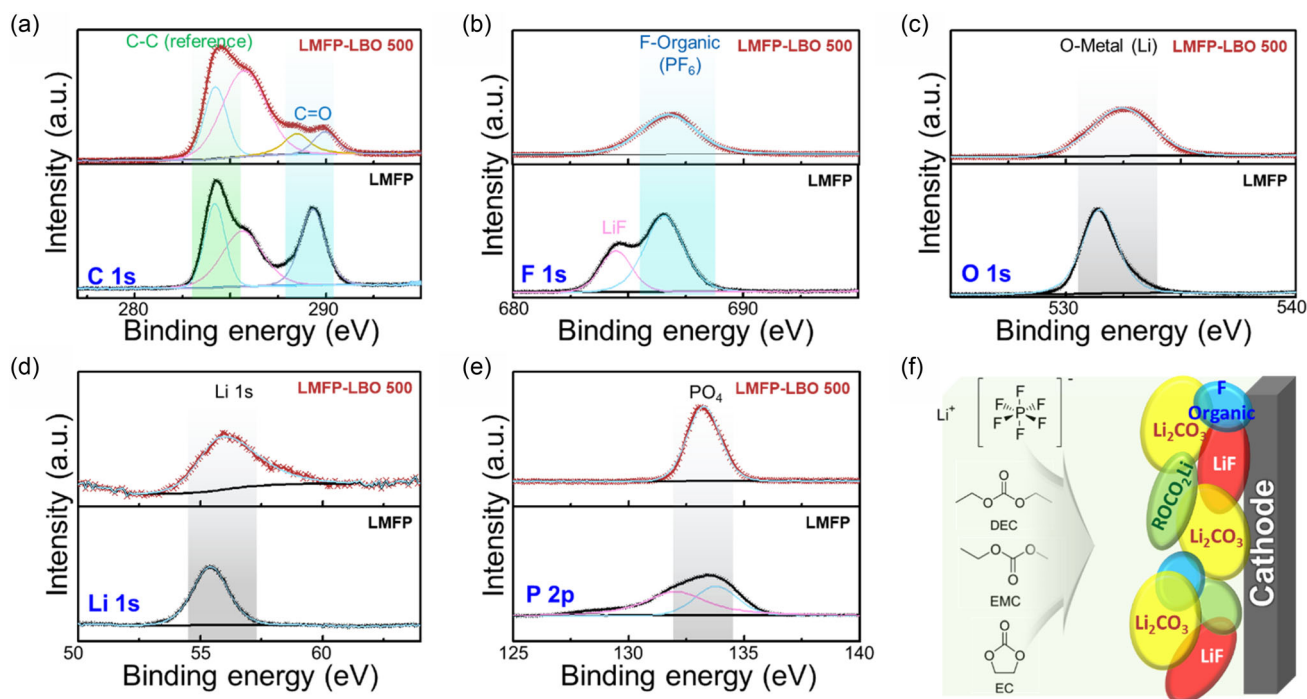
Batteries & Supercaps

Research Article
doi.org/10.1002/batt.202500207

Chemistry Europe
European Chemical
Societies Publishing

Figure 7. XPS spectra of after-cycled LMFP and LMFP-LBO 500 electrode: a) C 1s, b) F 1s, c) O 1s, d) Li 1s, e) P 2p spectra, and f) schematic illustration of the cathode interface layer composition.

preserving both the crystallographic integrity and the local chemical environment of phosphate groups during extended cycling.

In summary, as illustrated in Figure 7f, the use of a LiPF$_6$-based electrolyte composed of EC, EMC, and DEC facilitates the accumulation of decomposition products such as Li$_2$CO$_3$, ROCO$_2$Li, LiF, and fluorinated organic species, leading to the formation of a protective CEI layer even with artificial LBO coating. The CEI layer, derived from the electrolyte, co-deposits with the LBO layer, collectively enhancing the cycling stability of LMFP. However, similar to conventional cells, an increase in charge transfer resistance is observed after the cycles (Figure 5e). Despite this, the formation of this protective layer effectively mitigates electrolyte decomposition and safeguards the cathode material (no structural degradation after the 1000 cycles, Figure S15 and S16, Supporting Information), thereby improving the electrochemical performance and long-term stability of the system. Although the formation of a CEI layer on LMFP-LBO500 after prolonged cycling is clearly supported by EIS (Figure 5e) and XPS analyses (Figure 7), the post-cycling XRD patterns (Figure S15, Supporting Information) show negligible changes in either background intensity or peak shape. This observation is attributed to the extremely thin and amorphous nature of the CEI, which renders it virtually undetectable by X-ray diffraction. The low mass fraction and absence of long-range crystallinity prevent the CEI components from producing discernible features in the bulk XRD signal. These findings underscore the importance of employing surface-sensitive techniques such as XPS and EIS, in conjunction with bulk structural characterization, to comprehensively evaluate interfacial evolution during cycling.

3. Conclusion

In this study, we successfully demonstrated the enhanced electrochemical performance and cycling stability of LMFP through the application of an amorphous LBO coating. Using the soft-BV method, we confirmed that LBO exhibits excellent lithium-ion conductivity, establishing it as an effective coating material for LMFP. A comparative analysis of amorphous and crystalline LBO revealed that the amorphous phase provides superior electrochemical performance because of its structural advantages. Comprehensive structural, morphological, spectroscopic, thermal, and electrochemical characterizations demonstrated that the disordered nature of amorphous LBO reduces Coulomb repulsion, thereby lowering the energy barrier for lithium-ion migration. Consequently, the lithium intercalation ratio is enhanced even at high current densities. Additionally, the LBO coating serves as a physical barrier that suppresses Mn dissolution from the LMFP structure, thereby mitigating the effects of Jahn-Teller distortion. These improvements collectively enhance lithium-ion conductivity and structural stability, resulting in superior cycle retention and high-rate capability. Consequently, LMFP-LBO500 exhibited significantly enhanced electrochemical performance, demonstrating excellent capacity retention of 94.6% after 1000 cycles and improved rate capability. These findings underscore the critical role of amorphous LBO in stabilizing LMFP by suppressing Mn dissolution and minimizing Jahn-Teller distortion while enhancing electrochemical performance. This approach offers a scalable and practical strategy for developing high-performance, long-cycle-life lithium-ion battery cathodes, presenting promising potential for next-generation energy storage applications.

Batteries & Supercaps

Research Article
doi.org/10.1002/batt.202500207

Chemistry Europe
European Chemical
Societies Publishing

4. Experimental Section

Materials and Electrochemical Characterization

The bare LMFP and LBO-coated LMFP (baked at 500 °C and 700 °C) were analyzed using field-emission transmission electron microscopy (TEM, FEI Themis Z), field-emission scanning electron microscopy (FE-SEM, Hitachi SU-8020) with an EDX attachment, and inductively coupled plasma optical emission spectrometry (ICP-OES, Varian 700-ES), respectively.

All electrochemical experiments were conducted using 2032-type coin cells. The working electrode comprised the synthesized cathode material (LMFP + LBO), a conductive material, and a binder in a weight ratio of 8:1:1. Super C65 carbon black (Timcal—Graphite & Carbon) served as the conductive material, while polyvinylidene fluoride (Kureha Corp.) was used as the binder. All components were mixed and dispersed in N-methyl-2-pyrrolidone (Sigma-Aldrich) solution, then coated onto 20 μm aluminum foil. The coated electrodes were punched and assembled into coin cells under an inert atmosphere inside a glove box. The electrolyte solution consisted of 1.3M $LiPF_6$ in a 3EC/5EMC/2DEC solution, with polypropylene used as the separator, and lithium metal as the anode.

Structural Analysis

XRD measurements were conducted using Cu Kα radiation on a Mini-Flex 600 (Rigaku). Rietveld refinements for the samples were performed using the GSAS[43] program, utilizing the initial structural model from the Materials Project.[44]

To investigate lithium-ion diffusion pathways and migration barriers, the Soft BV program[25,26] was utilized for bond softness analysis. The resulting Li diffusion pathways are highlighted in sky blue, and visualizations of both the crystal structure and diffusion pathways were created using the VESTA3 program.[45,46]

Conflict of Interest

The authors declare no conflict of interest.

Data Availability Statement

The data that support the findings of this study are available from the corresponding author upon reasonable request.

[1] M. Armand, J.-M. Tarascon, *Nature* **2008**, *451*, 652.
[2] J. Xiang, Y. Wei, Y. Zhong, Y. Yang, H. Cheng, L. Yuan, H. Xu, Y. Huang, *Adv. Mater.* **2022**, *34*, 2200912.
[3] H. Chang, Y.-R. Wu, X. Han, T.-F. Yi, *Energy Mater.* **2021**, *1*, 100003.
[4] P. Nzereogu, A. Omah, F. Ezema, E. Iwuoha, A. Nwanya, *Appl. Surf. Sci. Adv.* **2022**, *9*, 100233.
[5] L. Zhu, L. Fu, K. Zhou, L. Yang, Z. Tang, D. Sun, Y. Tang, Y. Li, H. Wang, *Chem. Rec.* **2022**, *22*, e202200128.
[6] M. A. Kebede, *Curr. Opin. Electrochem.* **2023**, *39*, 101261.
[7] L. Britala, M. Marinaro, G. Kucinskis, *J. Energy Storage* **2023**, *73*, 108875.
[8] S.-P. Chen, D. Lv, J. Chen, Y.-H. Zhang, F.-N. Shi, *Energy Fuels* **2022**, *36*, 1232.
[9] B. Ramasubramanian, S. Sundarrajan, V. Chellappan, M. Reddy, S. Ramakrishna, K. Zaghib, *Batteries* **2022**, *8*, 133.
[10] S. Liu, Y. Wang, H. Du, Y. Li, Y. Wang, G. Wang, J. Wang, Q. Liao, X. Guo, H. Yu, *Adv. Energy Mater.* **2024**, *15*, 2404459.
[11] L. Yang, W. Deng, W. Xu, Y. Tian, A. Wang, B. Wang, G. Zou, H. Hou, W. Deng, X. Ji, *J. Mater. Chem. A* **2021**, *9*, 14214.
[12] A. Nekahi, A. K. MR, X. Li, S. Deng, K. Zaghib, *Mater. Sci. Eng. R Rep.* **2024**, *159*, 100797.
[13] S. Li, H. Zhang, Y. Liu, L. Wang, X. He, *Adv. Funct. Mater.* **2024**, *34*, 2310057.
[14] Z. Lv, M. Li, J. Lin, J. Luo, B. Wu, R. Hong, S. C. Cao, *J. Solid State Electrochem.* **2024**, *28*, 577.
[15] Z. Li, Y. You, Z. Zhu, L. Wang, S. Ou, J. Xu, M. Yuan, *Appl. Surf. Sci.* **2025**, *682*, 161689.
[16] H. Xiong, Z. Zhang, J. Dai, P. Zhao, K. He, J. Gao, Q. Wu, B. Wang, *ChemElectroChem* **2024**, *11*, e202400440.
[17] Y. Li, X. Liu, D. Ren, H. Hsu, G.-L. Xu, J. Hou, L. Wang, X. Feng, L. Lu, W. Xu, *Nano Energy* **2020**, *71*, 104643.
[18] J. Cho, Y. J. Kim, B. Park, *J. Electrochem. Soc.* **2001**, *148*, A1110.
[19] J. S. Park, A. U. Mane, J. W. Elam, J. R. Croy, *Chem. Mater.* **2015**, *27*, 1917.
[20] W. Chang, J.-W. Choi, J.-C. Im, J. K. Lee, *J. Power Sources* **2010**, *195*, 320.
[21] U. Nisar, N. Muralidharan, R. Essehli, R. Amin, I. Belharouak, *Energy Storage Mater.* **2021**, *38*, 309.
[22] M. S. Chae, *J. Solid State Chem.* **2024**, *337*, 124788.
[23] S. Hashigami, K. Yoshimi, Y. Kato, H. Yoshida, T. Inagaki, M. Haruta, M. Hashinokuchi, T. Doi, M. Inaba, *Chem. Select* **2019**, *4*, 8676.
[24] W. Mo, Z. Wang, J. Wang, X. Li, H. Guo, W. Peng, G. Yan, *Chem. Eng. J.* **2020**, *400*, 125820.
[25] S. Adams, *Acta Crystallogr. B* **2001**, *57*, 278.
[26] H. Chen, L. L. Wong, S. Adams, *Acta Crystallogr. B* **2019**, *75*, 18.
[27] Z. Lu, S. Hao, M. Aykol, Z. Yao, C. Wolverton, *Chem. Mater.* **2024**, *36*, 10205.
[28] W. Dong, Z. Liu, M. Xie, Y. Chen, W. Ma, S. Liang, Y. Bai, F. Huang, *Adv. Mater.* **2024**, *36*, e2311424.
[29] W. Dong, F. Huang, *EScience* **2024**, *4*, 100158.
[30] W. Dong, Y. Zhao, X. Wang, X. Yuan, K. Bu, C. Dong, R. Wang, F. Huang, *Adv. Mater.* **2018**, *30*, e1801409.
[31] W. Dong, Y. Zhao, M. Cai, C. Dong, W. Ma, J. Pan, Z. Lv, H. Dong, Y. Dong, Y. Tang, F. Huang, *Small* **2023**, *19*, 2207074.
[32] D. Pan, Z. Liu, C. Li, R. Wan, J. Wang, J. Chen, D. Wang, J. Liu, Y. Zhang, J. Yi, *Particuology* **2024**, *92*, 278.
[33] C. C. Zhang, X. Gao, B. Yilmaz, *Catalysts* **2020**, *10*, 1327.
[34] Z. Zhang, X. Ouyang, J. Wang, X. Guo, *J. Porous Mater.* **2024**, *31*, 2139.
[35] I. Jum'h, M. Al-Addous, H. Al-Taani, M. El-Sadik, N. Ayoub, *Dig. J. Nanomater. Biostruct.* **2017**, *12*, 589.
[36] J. Ding, D. Ji, Y. Yue, M. M. Smedskjaer, *Small* **2024**, *20*, 2304270.
[37] K. Xu, M. Yao, J. Chen, P. Zou, Y. Peng, F. Li, X. Yao, *J. Alloys Compd.* **2015**, *653*, 7.
[38] F. Tian, M. D. Radin, D. J. Siegel, *Chem. Mater.* **2014**, *26*, 2952.
[39] E. Hüger, L. Dörrer, J. Rahn, T. Panzner, J. Stahn, G. Lilienkamp, H. Schmidt, *Nano Lett.* **2013**, *13*, 1237.
[40] X. Lei, J. Wang, K. Huang, *J. Electrochem. Soc.* **2016**, *163*, A1401.
[41] J. Pan, Q. Zhang, J. Li, M. J. Beck, X. Xiao, Y.-T. Cheng, *Nano Energy* **2015**, *13*, 192.
[42] M. Sonoki, M. Matsui, N. Imanishi, *J. Electrochem. Soc.* **2019**, *166*, A3593.
[43] B. H. Toby, *J. Appl. Crystallogr.* **2001**, *34*, 210.
[44] A. Jain, S. P. Ong, G. Hautier, W. Chen, W. D. Richards, S. Dacek, S. Cholia, D. Gunter, D. Skinner, G. Ceder, K. A. Persson, *APL Mater.* **2013**, *1*, 011002.
[45] K. Momma, F. Izumi, *J. Appl. Crystallogr.* **2011**, *44*, 1272.
[46] K. Momma, F. Izumi, *J. Appl. Crystallogr.* **2008**, *41*, 653.